

Activation of Cloud Droplets in Bin-Microphysics Simulation of Shallow Convection

Andrzej A. WYSZOGRODZKI¹,
Wojciech W. GRABOWSKI¹, and Lian-Ping WANG²

¹National Center for Atmospheric Research, Boulder, CO, USA
e-mail: andii@ucar.edu (corresponding author)

²Department of Mechanical Engineering,
University of Delaware, Newark, DE, USA

Abstract

This paper describes implementation of the warm-rain bin microphysics in a LES model based on the EULAG fluid flow solver. The bin-microphysics EULAG is applied to the case of shallow nonprecipitating tropical convection to investigate the impact of the secondary activation of cloud droplets above the cloud base. In a previous study applying the EULAG model with the double-moment bulk warm-rain microphysics scheme, the in-cloud activation was shown to have significant implications for the mean microphysical and optical characteristics of the cloud field. By contrasting the simulations with and without in-cloud activation as in the previous study, we show that the in-cloud activation has qualitatively similar but quantitatively smaller effect. In particular, the concentration of cloud droplets in the bin simulation without in-cloud activation decreases with height not as strongly as in corresponding simulations applying the double-moment bulk scheme.

Key words: shallow convection, cloud physics, bin microphysics, droplet activation.

1. INTRODUCTION

Microphysical properties of shallow convective clouds, such as subtropical stratocumulus and tropical shallow cumulus, are of significant importance for the

Earth climate and climate change. The size of cloud droplets within such clouds critically affects the amount of solar radiation reflected back to space, whereas removal of cloud water through precipitation processes can potentially affect such bulk cloud properties as the cloud fraction and cloud lifetime. These impacts are typically referred to as the first and the second indirect aerosol effects, respectively (*e.g.*, Twomey 1974, 1977, Albrecht 1989, Pincus and Baker 1994). The reference to aerosols in this context emphasizes the role of cloud condensation nuclei (CCN), small atmospheric aerosols involved in the formation of cloud droplets. For instance, differences in CCN are primarily responsible for the differences between clouds developing in clean marine and polluted continental environments. Because shallow convective clouds cover a large fraction of the Earth tropics and subtropics, they exert a significant control over the partitioning of the incoming solar radiative flux into energy reflected back to space and energy absorbed by the Earth climate system. They have been identified as playing the key role in the climate change and climate sensitivity (*e.g.*, Bony and Dufresne 2005).

The above arguments motivated a significant interest in understanding physical processes that shape the spectrum of cloud droplets and ability of shallow clouds to produce precipitation. Observational, theoretical, and modeling approaches have all been used in efforts to further understand of cloud dynamics and microphysics of shallow convective clouds and their coupling to other climate-related processes, such as surface-atmosphere exchange and radiative transfer, see a collection of recent reviews in Heintzenberg and Charlson (2009).

Recently, Slawinska *et al.* (2011; SGPM hereafter) conducted a study applying the Large Eddy Simulation (LES) – EULAG model coupled with the double-moment bulk warm-rain microphysics of Morrison and Grabowski (2007, 2008) and showed that the secondary activation of cloud droplets, that is, activation above the cloud base (referred to as in-cloud activation) plays an important role in shaping the microphysical properties of shallow convection clouds. Such a conclusion was reached by comparing simulations with in-cloud activation and simulations where the in-cloud activation was artificially suppressed. In particular, simulations with in-cloud activation reproduced the observed approximately constant-in-height mean concentration of cloud droplets (Gerber *et al.* 2008, Arabas *et al.* 2009) and resulted in significantly smaller sizes of cloud droplets (*cf.* Figs. 2 and 7 in SGPM). The latter also agreed with remote-sensing observations reported in McFarlane and Grabowski (2007; see Fig. 2 therein). The in-cloud activation was suggested to be important for mean droplet spectral characteristics, both in observations (*e.g.*, Warner 1969, Paluch and Knight 1984, Gerber 2006, McFarlane and Grabowski 2007) and in modeling studies (*e.g.*, Brenguier and Grabowski 1993, Su *et al.* 1998).

However, the double-moment bulk microphysics imposes significant limitations on the droplet spectra. In particular, the double-moment scheme is

incapable of predicting droplet spectra with spatially-variable width (because the width is assumed to only weakly depend on the droplet concentration, see eq. 2 in Morrison and Grabowski 2007) or bimodal spectra that should form in the process of in-cloud activation (see discussion in Brenguier and Grabowski 1993). In this paper we present an extension of the EULAG model to include the bin microphysics, focusing on the droplet activation and condensational growth only. The bin model is the same as used in Grabowski *et al.* (2011). It includes a traditional bin representation applying the spectral density function and an improved representation of CCN activation.

The next section provides a brief overview of the model formulation and its numerical implementation. Section 3 presents example of results focusing on the impact of in-cloud activation. Overall, bin model results are consistent with those reported in SGPM, but there are some quantitative differences. A brief summary of our results is presented in Section 4.

2. EULAG MODEL WITH BIN MICROPHYSICS

2.1 Analytic formulation

The analytic formulation of bin-microphysics EULAG model combines evolution equations for the fluid flow and representation of moist thermodynamics with size-resolving warm-rain microphysics. The fluid flow model was recently reviewed in Prusa *et al.* (2008), who also provided a comprehensive list of references. The anelastic momentum and continuity equations are written as

$$\frac{d\mathbf{v}}{dt} = \nabla\pi' - \mathbf{g}\frac{\theta'_d}{\bar{\theta}} + D_{\mathbf{v}}, \quad (1)$$

$$\nabla \cdot (\bar{\rho}\mathbf{v}) = 0, \quad (2)$$

where the total derivative is $\frac{d\psi}{dt} \equiv \frac{\partial\psi}{\partial t} + \frac{1}{\bar{\rho}}\nabla \cdot (\bar{\rho}\mathbf{u}\psi)$; \mathbf{v} is the three-dimensional velocity vector; $\pi' = p'/\bar{p}$ is the normalized pressure perturbation (derived applying the anelastic continuity equation (2)); θ_d is the density potential temperature (*e.g.*, Emanuel 1994, eq. 4.3.6) usually applied in cloud modeling as $\theta_d = \theta + \bar{\theta}(\epsilon q_v - q_c)$ (where $\epsilon + 1 \equiv R_v/R_d$ is the ratio of the gas constants for water vapor and dry air, θ is the potential temperature, and q_v and q_c are the water vapor and condensed water mixing ratios, respectively); and $\theta'_d \equiv \theta_d - \theta_{de}$, where θ_{de} is the ambient profile of the density potential temperature (typically taken as $\theta_{de} = \theta_e + \bar{\theta}\epsilon q_{ve}$). The overbar denotes a dry reference state (*i.e.*, $\bar{\rho}$ and $\bar{\theta}$), whereas prime denotes deviations from the hydrostatically (and geostrophically in the case of a rotating system) balanced ambient state (\mathbf{v}_e , θ_e , q_{ve}). Finally, $D_{\mathbf{v}}$ represents additional momentum sources/sinks not explicitly represented in (1), such as the Coriolis term for the rotating system,

turbulent momentum transport, gravity wave absorbers in the vicinity of model boundaries, *etc.* Representation of the turbulent transports requires prediction of the subgrid-scale turbulent kinetic energy (TKE) from which turbulent exchange coefficients for momentum and all model scalars are derived as detailed in Margolin *et al.* (1999).

The moist warm-rain bin microphysics consists of conservation equations for the perturbation potential temperature θ' (*cf.* Smolarkiewicz *et al.* 2001, Grabowski and Smolarkiewicz 2002), the water vapor mixing ratio q_v , and the condensed water mixing ratio q_c represented by the spectrum of water drops. The latter is formulated using the spectral density function $f(\mathbf{x}, r) \equiv dn(\mathbf{x}, r)/dr$, where $n(\mathbf{x}, r)$ is the concentration (per unit mass of dry air as the mixing ratio) of drops smaller than r (*i.e.*, the cumulative number concentration) at a physical location \mathbf{x} . In this approach, activation of CCN provides a source of cloud droplets at the small-size end of the spectral representation and subsequent growth of cloud droplets shifts the spectral density function toward larger sizes (see discussions in Grabowski and Wang 2009, Grabowski *et al.* 2011 and references therein). The equations for θ' and q_v are:

$$\frac{d\theta'}{dt} = -\mathbf{v} \cdot \nabla \theta_e + \frac{L_v}{\Pi c_p} C + D_\theta, \quad (3)$$

$$\frac{dq_v}{dt} = -C + D_{q_v}, \quad (4)$$

where L_v and c_p are the latent heat of condensation and specific heat of air at constant pressure, respectively; $\Pi = (p_e/p_0)^{R/c_p}$ is the ambient Exner function (p_e is the ambient pressure profile and $p_0 = 1000$ hPa); C is the condensation/evaporation rate of cloud droplets and rain drops; and D terms represent sources/sinks not explicitly represented in equations, similarly as in (1). The spectral density function f is represented by the equation:

$$\frac{\partial f}{\partial t} + \frac{1}{\bar{\rho}} \nabla \cdot (\bar{\rho}[\mathbf{v} - \mathbf{k}v_t(r)]f) + \frac{\partial}{\partial r} \left(\frac{dr}{dt} f \right) = \left(\frac{\partial f}{\partial t} \right)_{\text{act}} + \left(\frac{\partial f}{\partial t} \right)_{\text{coal}} + D_f, \quad (5)$$

where $v_t(r)$ is the sedimentation velocity of droplets and drops (calculated based on Beard 1976), and \mathbf{k} is the unit vector in the vertical direction. The third term on the left-hand-side represents growth of cloud droplets by the condensation of water vapor (or their evaporation in subsaturated air) which are represented by the advection of f in the radius space, with dr/dt being the rate of change of the droplet/drop radius r due to condensation or evaporation. The rate dr/dt depends on the predicted super- or subsaturation and includes ventilation effects essential for evaporation of large cloud droplets and raindrops. The first term on the rhs (*i.e.*, the one with the subscript *act*) represents the cloud droplet activation (*i.e.*, the initial source of cloud droplets). Droplet activation is simulated

applying the Twomey approach where the concentration of activated droplets depends on the local value of the supersaturation (Twomey 1959, see discussion in Grabowski *et al.* 2011). The second term on the rhs (*i.e.*, the one with the subscript *coal*) represents growth of cloud droplets and precipitation drops by collision/coalescence. As first derived by Smoluchowski (1916) this term includes (i) the source of drops of a given mass m due to collisions of drops whose combined mass is equal to m , and (ii) the sink of drops due to collisions of drops with mass m with all other drops. The last term represents contribution of the turbulent transport in the physical space. Note that for simulations discussed in this paper the collision/coalescence term is excluded from the model as we focus on droplet activation and condensational growth only.

The bin-microphysics model requires prediction of two additional variables. The first one is the concentration of activated cloud droplets N_{act} . Without collision/coalescence, N_{act} is simply the local total concentration of cloud droplets $N \equiv \int f dr$. When collision/coalescence is allowed, however, N_{act} may differ significantly from N and needs to be predicted to allow appropriate representation of additional in-cloud activation. This equation can be compactly written as

$$\frac{dN_{\text{act}}}{dt} = D_{N_{\text{act}}}, \quad (6)$$

where $D_{N_{\text{act}}}$ is the tendency due to cloud droplet activation and deactivation (*i.e.*, complete evaporation) as well as the turbulent transport in the physical space. The second predicted variable is the absolute supersaturation $\delta \equiv q_v - q_{v_s}$, where q_{v_s} is the saturated water vapor mixing ratio (see the appendix in Morrison and Grabowski 2008). The solution of the supersaturation equation is needed for the adjustment of the temperature and water vapor fields near cloud boundaries (see discussion in Grabowski and Morrison 2008) to avoid unphysical values of the supersaturation field derived from the predicted temperature and water vapor fields as first noted in Grabowski (1989). These numerical artifacts impact the droplet activation as shown in Grabowski and Morrison (2008). However, only a simplified form of the supersaturation equation is solved omitting the tendencies due to subgrid-scale parameterized mixing (*cf.* appendix in Morrison and Grabowski 2008):

$$\frac{d\delta}{dt} = Bw - \frac{\delta}{\tau}, \quad (7)$$

where B is the temperature and pressure dependent coefficient, w is the local vertical velocity, and $\tau \sim 1/\int r f dr$ is the phase relaxation time scale (see appendix in Morrison and Grabowski 2008).

2.2 Finite-difference implementation

The fluid flow model applies the second-order accurate nonoscillatory forward-in-time (NFT) approach (Smolarkiewicz and Grabowski 1990, Smolarkiewicz and Szmelter 2009). The momentum equation is formally written as

$$\psi_i^{n+1} = LE_i(\tilde{\psi}) + 0.5\Delta t R_i^{n+1} \equiv \hat{\psi}_i + 0.5\Delta t R_i^{n+1}, \quad (8)$$

where ψ_i^{n+1} is the solution sought at the grid point (t^{n+1}, \bar{x}_i) ; $\tilde{\psi} \equiv \psi^n + 0.5\Delta t R^n$; R is the associated right-hand-side (rhs) forcing terms; and LE denotes a two-time-level NFT transport operator, the advection scheme MPDATA (Smolarkiewicz 2006). The thermodynamic equations (θ , q_v , and $f^{(j)}$, with the latter representing the spectral density function for the drop bin j , $j = 1, \dots, \mathcal{N}$, where \mathcal{N} is the total number of bins) are simulated using the uncentered (*i.e.*, first-order-in-time) scheme which can be written as

$$\psi_i^{n+1} = LE_i(\psi^n + \Delta t R^n). \quad (9)$$

For the bin microphysics, we apply the bin setup corresponding to one of the bin grids considered in Grabowski *et al.* (2011, Section 3.3), namely the grid with the total number of bins $\mathcal{N} = 72$. However, since we consider a non-precipitating shallow convection and focus on the droplet activation and condensational growth as SGPM, the grid can exclude drizzle and raindrops. Consequently, the number of bins is reduced to $\mathcal{N} = 32$, with the bin grid only extending up to a droplet radius of about 50 μm . Note that this leads to substantial (close to a half) savings of computational resources when compared to simulations using $\mathcal{N} = 72$. All other aspects of the bin-microphysics model are exactly the same as described in Grabowski *et al.* (2011).

3. BIN-MICROPHYSICS SIMULATIONS OF THE BOMEX CASE

The bin-microphysics EULAG LES is applied in simulations of nonprecipitating trade-wind shallow convection observed during the Barbados Oceanographic and Meteorological Experiment (BOMEX; Holland and Rasmusson 1973) and used in the model intercomparison study described in Siebesma *et al.* (2003). In the BOMEX case, the 1.5-km-deep trade-wind convection layer overlays 0.5-km-deep mixed layer near the ocean surface and is covered by 0.5-km-deep trade-wind inversion. The cloud cover is about 10% and quasi-steady conditions are maintained by the prescribed large-scale subsidence, large-scale moisture advection, surface heat fluxes, and radiative cooling. In the current experiments a grid size of $128 \times 128 \times 151$ is implemented with horizontal and vertical gridlengths of 50 and 20 m, respectively, as in SGPM. The time step is $\Delta t = 1.5$ s. The model is run for 6 hours as in Siebesma *et al.* (2003) and results from the last hour are used in the analysis. As in SGPM, we compare two simulations, one applying the standard model, and the

second one where the activation of cloud droplets above the height of 700 m is suppressed.

Similarly to SGPM, the simulations consider CCN characteristics corresponding to pristine and polluted aerosols. However, because of the different representation of the CCN activation in the bin microphysics compared to SGPM, aerosol characteristics are assumed following Rasmussen *et al.* (2002). For the polluted case, the concentration of activated CCN, N_{CCN} (in mg^{-1}), is given by

$$N_{\text{CCN}} = \begin{cases} 3.16 \times 10^6 S^4 & \text{if } S < 0.1 \\ 1000 S^{0.5} & \text{if } 0.1 < S < 1.0 \\ 1000 & \text{if } S > 1.0 \end{cases} \quad (10)$$

whereas for the pristine case it is:

$$N_{\text{CCN}} = \begin{cases} 4.78 \times 10^5 S^4 & \text{if } S < 0.1 \\ 120 S^{0.4} & \text{if } 0.1 < S < 1.0 \\ 120 & \text{if } S > 1.0 \end{cases} \quad (11)$$

where S (in % in the above formulas) is the supersaturation over flat water surface. These formulas are used in the model as discussed in Grabowski *et al.* (2011). Overall, different representation of droplet activation leads to higher droplet concentrations in the bin model compared to SGPM (*e.g.*, 30-40 mg^{-1} in SGPM *versus* 50-70 mg^{-1} here for the pristine cases; 200-250 mg^{-1} in SGPM *versus* 350-450 mg^{-1} here for the polluted cases). However, these differences are unimportant for mostly qualitative comparison of the double-moment and bin model results. It should be also pointed out that, as far as the subgrid-scale cloud-environment mixing is concerned, the formulation of the bin model corresponds to the homogeneous subgrid-scale mixing. Based on SGPM results, we do not anticipate large differences between homogeneous and extremely inhomogeneous subgrid-scale mixing scenarios, and consequently decided not to implement the extremely-inhomogeneous mixing logic for the bin microphysics (see Fig. 5 in Grabowski *et al.* 2010 that illustrates how the extremely inhomogeneous mixing can be implemented; see also Hill *et al.* 2009).

Figure 1 compares snapshot examples of the 3D distribution of cloud fields projected on the vertical plane at time of 6 hrs for the pristine simulations with and without in-cloud activation. The figure identifies areas where the CCN activation takes place by marking cloudy volumes with $q_c > 0.05 \text{ g kg}^{-1}$ and the cloud droplet concentration tendency due to activation larger than 1 $(\text{mg s})^{-1}$. As the figure documents, the maximum activation occurs at the cloud base with the peak at the height of 640 m. In the case where the activation is allowed above the 700 m, additional activation takes place in patchy areas that extend across the entire cloud depth. As in SGPM, the spatial pattern of these areas changes in space and time as individual clouds evolve (not shown).

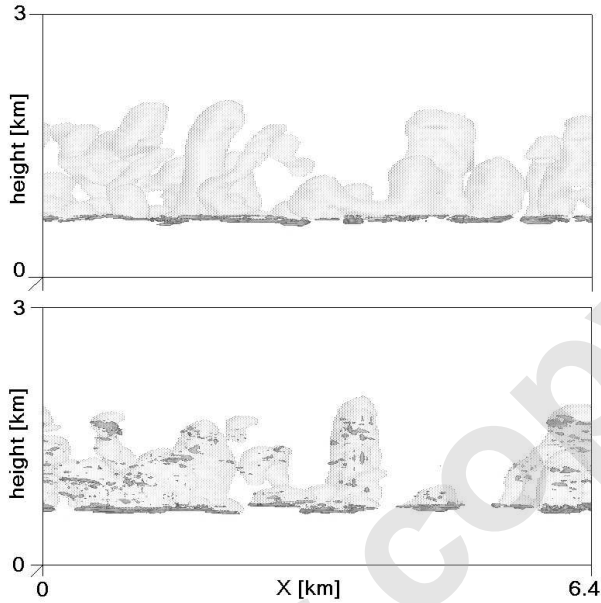


Fig. 1. Snapshot of cloud water mixing ratio (light shaded isosurface) of $q_c = 0.05 \text{ g kg}^{-1}$ and the activation tendency larger than 1 (mg s)^{-1} (a patchy dark shaded areas). Top/bottom panel is for suppressed/active in-cloud activation.

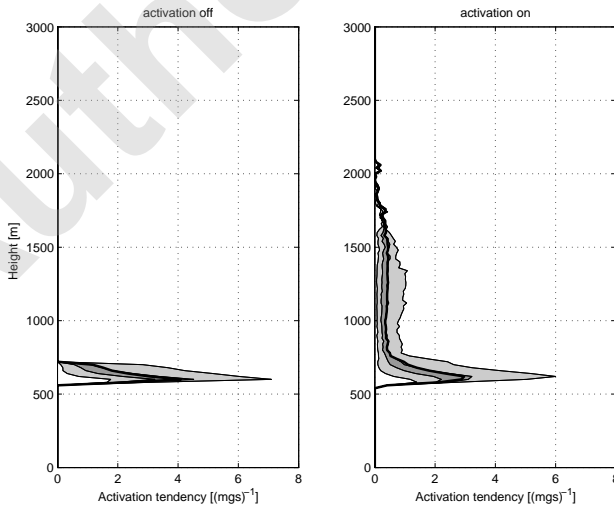


Fig. 2. Percentile distribution of space and time averaged activation tendency in areas where $q_c > 0.01 \text{ g kg}^{-1}$ for the pristine case. The light shading represents values for 10-40% and 60-90% ranges; the dark shading is for 40-60% range. The black line is the mean value. Left/right panel is for simulations without/with in-cloud activation.

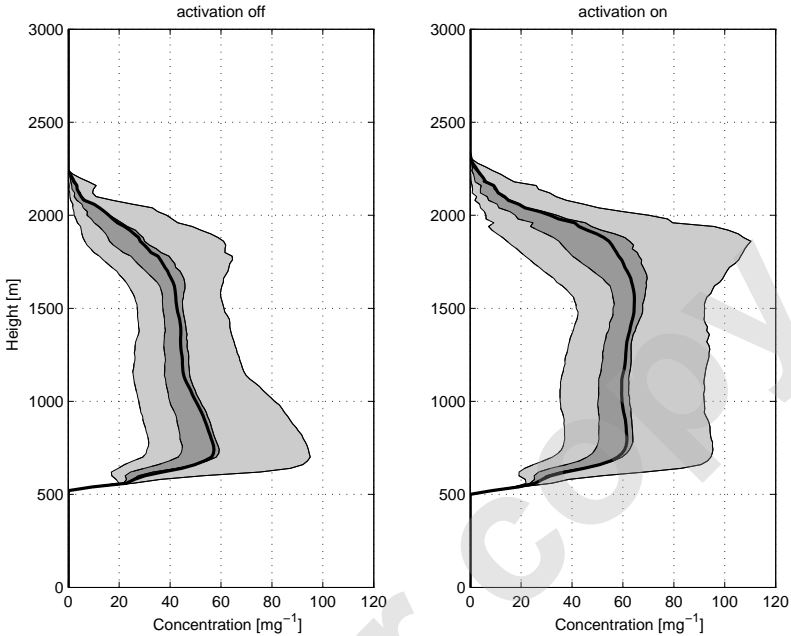


Fig. 3. As Figure 2, but for the cloud droplet concentration in the pristine case.

The space-and-time averaged activation tendency in the two pristine simulations within the areas of cloudy points ($q_c > 0.01 \text{ g kg}^{-1}$) is presented in Fig. 2. The time averaging is done by computing statistics from the last simulation hour separated by 5 min intervals. The peak at the cloud base is identified as well as additional activation above the cloud base (up to height of 1700 m) in the simulation with in-cloud activation. The in-cloud activation (defined for quantitative analysis as activation above the height of 700 m) contribute to about 40% of the total activation, which agree with SGPM results.

Figures 3 and 4 show the percentile distributions of the droplet concentration in the pristine and polluted cases, respectively, as a function of height. The mean concentrations (about 70 and 350 mg^{-1} for pristine and polluted, respectively) are approximately constant in cases with in-cloud activation, but they decrease with height in a similar manner when in-cloud activation is suppressed. The bin-model results are broadly consistent with SGPM (Fig. 2 therein, note that only profiles of the mean value was shown in SGPM). However, reduction of droplet concentration in no-in-cloud-activation cases is smaller in bin simulations compared to the double-moment simulations of SGPM. This impacts other quantities as discussed below. The width of the percentile distribution tends to increase with height in simulations with in-cloud activation, whereas the opposite trend is apparent in the no-in-cloud-activation simulations.

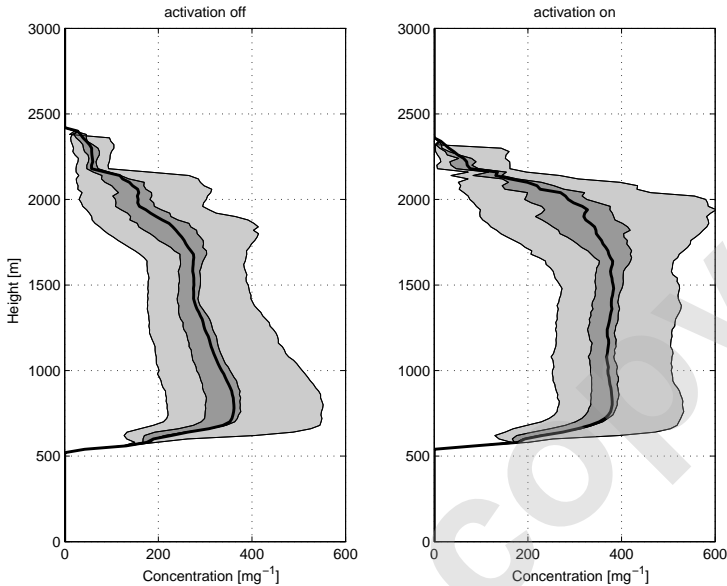


Fig. 4. As Figure 3, but for the polluted case.

The mean droplet spectra of the pristine simulation, at selected levels above 700 m (*i.e.*, 740, 1040, 1340, and 1540 m) are shown in Fig. 5. At each height, the spectrum is averaged over the cloudy points within model domain and over four snapshots from the last 15 min of the simulation (at each height, spatially-averaged spectra for different snapshots differ little; not shown). The difference between simulations with and without in-cloud activation appears rather small as far as the position of the spectral maximum is concerned. The simulation without in-cloud activation leads to formation of significant concentrations of larger droplets and reduced concentrations of smaller ones (note that dark bars in the figure are hidden behind white bars for droplet sizes to the left of the maximum). The former most likely results from enhanced droplet growth in regions with diluted concentrations, and the latter – from the lack of in-cloud activation that provides the source of small droplets when in-cloud activation is allowed.

Careful analysis of model results allows finding bimodal spectra in close proximity of grid points with in-cloud activation, *i.e.*, in regions above and downwind to the local in-cloud activation maximum. This is illustrated in Fig. 6 that shows cloud droplet spectra at selected heights (680, 1040, 1340, and 1540 m) in the pristine simulation. At each of these heights, the spectrum comes from a single cloudy location one level above the grid point where the local maximum activation occurs. Bimodality of the droplet spectra is apparent in each panel, especially at height 680 m (which is 40 m above level of maxi-

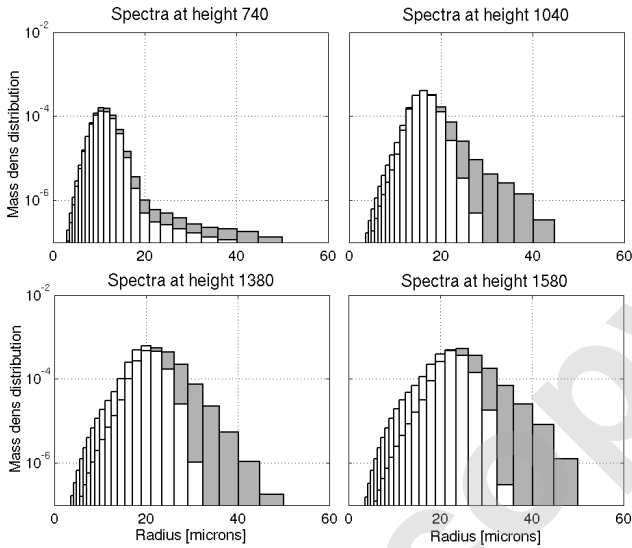


Fig. 5. Average droplet spectra for pristine simulations at four heights. Spectra are computed for a set of four snapshots from the last 15 min of the simulations, and averaged horizontally at each height within the areas with $q_c > 0.01 \text{ g kg}^{-1}$. The white and dark bars represent spectra with and without in-cloud activation, respectively. Note that dark bars are hidden behind white bars for droplet sizes to the left of the maximum.

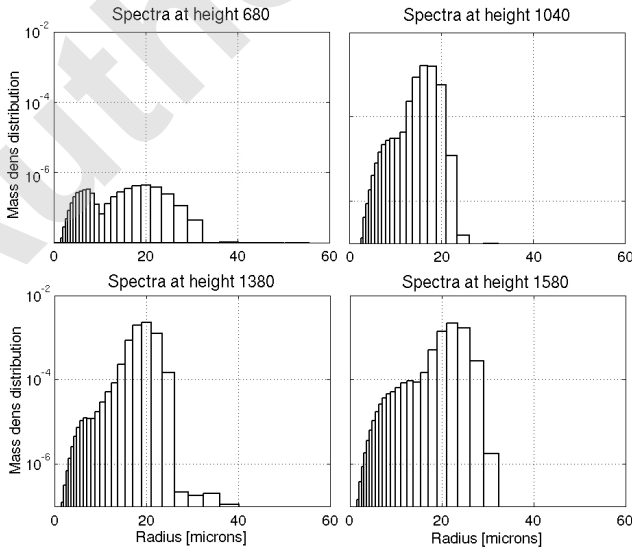


Fig. 6. Examples of droplet spectra just above the grid point with the maximum activation tendency at a given height for pristine simulation at the final time step.

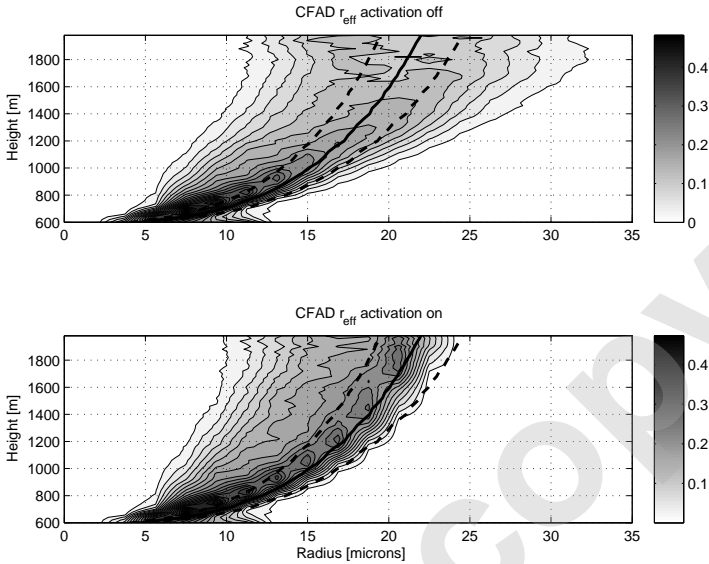


Fig. 7. CFADs of the effective radius for each pristine simulation in areas where $q_c > 0.01 \text{ g kg}^{-1}$. The adiabatic radii for cloud base concentrations of 50 and 100 mg^{-1} (representing 10% and 90% concentration percentiles, respectively) are shown by dashed lines. The adiabatic radius for the mean concentrations of 70 mg^{-1} is shown by solid line.

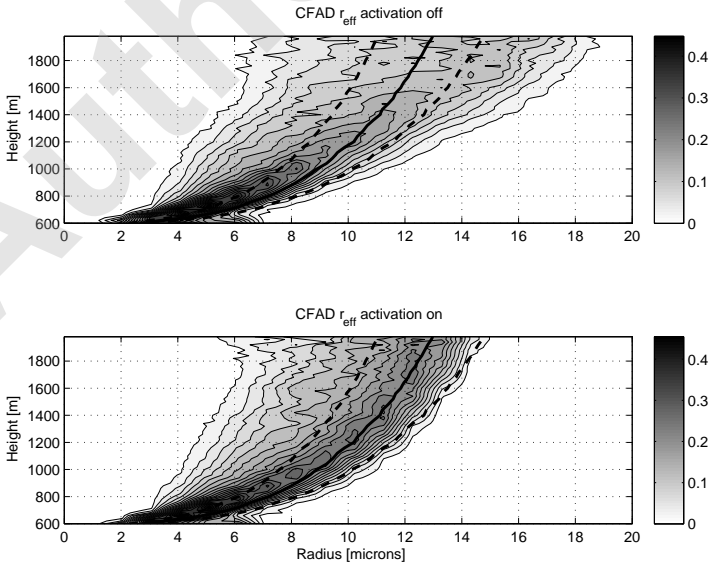


Fig. 8. As Figure 7, but for the polluted case, with the adiabatic radii for cloud base concentrations of 230, 340, and 550 mg^{-1} .

mum activation) where both peaks have similar maxima of mass densities and are well separated in the bin space. The secondary peak of the distribution is located to the left of the primary spectra peak at larger sizes. The primary peak shifts towards larger sizes as the height increases and seems to correspond to peaks of the averaged spectra shown in Fig. 5.

Finally, Figs. 7 and 8 show CFADs (contoured frequency by altitude diagrams) of the effective radius for pristine and polluted simulations, respectively. In both figures, the adiabatic radius is shown by dashed lines for two borderline droplet concentrations typical for the cloud-base activation: 50 and 100 mg^{-1} in the pristine case, and 230 and 550 mg^{-1} in polluted case. The mean adiabatic radius representing concentrations of 70 mg^{-1} for pristine and 340 mg^{-1} for polluted case is shown by the continuous line. As expected, the effective radii tend to be significantly smaller in the polluted case than in the pristine case (*e.g.*, the mean radius at the height of 1.6 km is around 12 μm for the polluted case *versus* 20 μm for the pristine case). As in SGPM, excluding in-cloud droplet activation leads to a significant shift of CFADs towards larger radii. Although the impact of in-cloud activation in the bin microphysics is different when compared to the double-moment bulk scheme (see Fig. 7 in SGPM for comparison), the salient outcomes of suppressing in-cloud activation are apparent. These include slightly wider frequency distributions and presence of larger droplets, especially at higher levels, when the in-cloud activation is suppressed.

4. SUMMARY

We replaced the double-moment bulk microphysics scheme by a bin scheme in EULAG simulations of nonprecipitating shallow tropical convection. We show that previous conclusions concerning CCN activation above the cloud base, the in-cloud activation, and its impact on cloud microphysical properties apply to the bin microphysics results as well. However, the effects of in-cloud activation are not as pronounced as when the double-moment bulk scheme is used in SGPM. In particular, the averaged droplet spectra at a given height are similar in simulations with and without droplet activation, which is arguably a result of spectral changes associated with cloud water evaporation in diluted regions. The bin microphysics does produce bimodal droplet spectra in regions of in-cloud activation, a feature suggested previously by high-resolution bin simulations reported in Brenguier and Grabowski (1993). Because of the underlying assumptions, the bulk double-moment microphysics scheme is not able to produce bimodal spectra. This apparently has a rather small impact on model results as the bin and bulk microphysics results qualitatively agree, although a smaller dilution of droplet concentration is simulated in the bin-microphysics no-in-cloud-activation simulations than in corresponding double-moment simulations in SGPM.

Acknowledgements. This work has been supported by the NSF through grants OCI-0904534 and OCI-0904449. Computer time at NCAR was provided by NSF MRI Grant CNS-0421498, NSF MRI Grant CNS-0420873, NSF MRI Grant CNS-0420985, NSF sponsorship of the National Center for Atmospheric Research, the University of Colorado, and a grant from the IBM Shared University Research (SUR) program. WWG was also partially supported by the NOAA grant NA08OAR4310543 and DOE ARM grant DE-FG02-08ER64574. National Center for Atmospheric Research is sponsored by the National Science Foundation.

References

- Albrecht, B.A. (1989), Aerosols, cloud microphysics, and fractional cloudiness, *Science* **245**, 4923, 1227-1230, DOI: 10.1126/science.245.4923.1227.
- Arabas, S., H. Pawlowska, and W.W. Grabowski (2009), Effective radius and droplet spectral width from in-situ aircraft observations in trade-wind cumuli during RICO, *Geophys. Res. Lett.* **36**, L11803, DOI: 10.1029/2009GL038257.
- Beard, K.V. (1976), Terminal velocity and shape of cloud and precipitation drops aloft, *J. Atmos. Sci.*, **33**, 5, 851-864, DOI: 10.1175/1520-0469(1976)033<0851:TVASOC>2.0.CO;2.
- Bony, S., and J.L. Dufresne (2005), Marine boundary layer clouds at the heart of tropical cloud feedback uncertainties in climate models, *Geophys. Res. Lett.* **32**, L20806, DOI: 10.1029/2005GL023851.
- Brenguier, J.-L., and W.W. Grabowski (1993), Cumulus entrainment and cloud droplet spectra: A numerical model within a two-dimensional dynamical framework, *J. Atmos. Sci.* **50**, 120-136., DOI: 10.1175/1520-0469(1993)050<0120:CEACDS>2.0.CO;2.
- Emanuel, K.A. (1994), *Atmospheric Convection*, Oxford University Press, New York, 580 pp.
- Gerber, H. (2006), Entrainment, mixing, and microphysics in RICO cumulus. **In:** *Proc. 12th Conf. on Cloud Physics, 9-14 July 2006, Madison, WI, USA*, Amer. Meteorol. Soc., P2.22.
- Gerber, H., G.M. Frick, J.B. Jensen, and J.G. Hudson (2008), Entrainment, mixing, and microphysics in trade-wind cumulus, *J. Meteorol. Soc. Jpn.* **86A**, 87-106, DOI: 10.2151/jmsj.86A.87.
- Grabowski, W.W. (1989), Numerical experiments on the dynamics of the cloud-environment interface: small cumulus in a shear-free environment, *J. Atmos. Sci.* **46**, 23, 3513-3541, DOI: 10.1175/1520-0493(1989)046<3513:NEOTDO>2.0.CO;2.
- Grabowski, W.W., and H. Morrison (2008), Toward the mitigation of spurious cloud-edge supersaturation in cloud models, *Month. Weather Rev.* **136**, 3, 1224-1234, DOI: 10.1175/2007MWR2283.1.

- Grabowski, W.W., and P.K. Smolarkiewicz (2002), A multiscale anelastic model for meteorological research, *Month. Weather Rev.* **130**, 4, 939-956, DOI: 10.1175/1520-0493(2002)130<0939:AMAMFM>2.0.CO;2.
- Grabowski, W.W., and L.-P. Wang (2009), Diffusional and accretional growth of water drops in a rising adiabatic parcel: effects of the turbulent collision kernel, *Atmos. Chem. Phys.* **9**, 7, 2335-2353, DOI: 10.5194/acp-9-2335-2009.
- Grabowski, W.W., O. Thouron, J.-P. Pinty, and J.-L. Brenguier (2010), A hybrid bulk-bin approach to model warm-rain processes, *J. Atmos. Sci.* **67**, 2, 385-399, DOI: 10.1175/2009JAS3155.1.
- Grabowski, W.W., M. Andrejczuk, and L.-P. Wang (2011), Droplet growth in a bin warm-rain scheme with Twomey CCN activation, *Atmos. Res.* **99**, 2, 290-301, DOI: 10.1016/j.atmosres.2010.10.020.
- Heintzenberg, J., and R.J. Charlson (eds.) (2009), *Clouds in the Perturbed Climate System: Their Relationship to Energy Balance, Atmospheric Dynamics, and Precipitation*, Struengmann Forum Report, MIT Press, Cambridge, MA, 597 pp.
- Hill, A.A., G. Feingold, and H. Jiang (2009), The influence of entrainment and mixing assumption on aerosol-cloud interactions in marine stratocumulus, *J. Atmos. Sci.* **66**, 5, 1450-1464, DOI: 10.1175/2008JAS2909.1.
- Holland, J.Z., and E.M. Rasmusson (1973), Measurements of the atmospheric mass, energy, and momentum budgets over a 500-kilometer square of tropical ocean, *Month. Weather Rev.* **101**, 44-55, DOI: 10.1175/1520-0493(1973)101<0044:MOTAME>2.3.CO;2.
- Margolin, L.G., P.K. Smolarkiewicz, and Z. Sorbjan (1999), Large-eddy simulations of convective boundary layers using nonoscillatory differencing, *Physica D* **133**, 390-397, DOI: 10.1016/S0167-2789(99)00083-4.
- McFarlane, S.A., and W.W. Grabowski (2007), Optical properties of shallow tropical cumuli derived from ARM ground-based remote sensing, *Geophys. Res. Lett.* **34**, L06808, DOI: 10.1029/2006GL028767.
- Morrison, H., and W.W. Grabowski (2007), Comparison of bulk and bin warm rain microphysics models using a kinematic framework, *J. Atmos. Sci.* **64**, 2839-2861, DOI: 10.1175/JAS3980.
- Morrison, H., and W.W. Grabowski (2008), Modeling supersaturation and subgrid-scale mixing with two-moment bulk warm microphysics, *J. Atmos. Sci.* **65**, 3, 792-812, DOI: 10.1175/2007JAS2374.1.
- Paluch, I.R., and C.A. Knight (1984), Mixing and the evolution of cloud droplet size spectra in a vigorous continental cumulus, *J. Atmos. Sci.* **41**, 11, 1801-1815, DOI: 10.1175/1520-0469(1984)041<1801:MATEOC>2.0.CO;2.
- Pincus, R., and M.B. Baker (1994), Effect of precipitation on the albedo susceptibility of clouds in the marine boundary layer, *Nature* **372**, 250-252, DOI: 10.1038/372250a0.
- Prusa, J.M., P.K. Smolarkiewicz, and A.A. Wyszogrodzki (2008), EULAG, a computational model for multiscale flows, *Comput. Fluids* **37**, 9, 1193-1207, DOI: 10.1016/j.compfluid.2007.12.001.

- Rasmussen, R.M., I. Geresdi, G. Thompson, K. Manning, and E. Karplus (2002), Freezing drizzle formation in stably stratified layer clouds: The role of radiative cooling of cloud droplets, cloud condensation nuclei, and ice initiation, *J. Atmos. Sci.* **59**, 4, 837-860, DOI: 10.1175/1520-0469(2002)059<0837:FDFISS>2.0.CO;2.
- Siebesma, A.P., C.S. Bretherton, A. Brown, A. Chlond, J. Cuxart, P.G. Duynkerke, H. Jiang, M. Khairoutdinov, D. Lewellen, C.-H. Moeng, E. Sanchez, B. Stevens, and D.E. Stevens (2003), A large eddy simulation intercomparison study of shallow cumulus convection, *J. Atmos. Sci.* **60**, 10, 1201-1219, DOI: 10.1175/1520-0469(2003)60<1201:ALESIS>2.0.CO;2.
- Slawinska, J., W.W. Grabowski, H. Pawlowska, and H. Morrison (2011), Droplet activation and mixing in large-eddy simulation of a shallow cumulus field, *J. Atmos. Sci.* (in print), DOI: 10.1175/JAS-D-11-054.1.
- Smolarkiewicz, P.K. (2006), Multidimensional positive definite advection transport algorithm: an overview, *Int. J. Numer. Meth. Fluids* **50**, 10, 1123-1144, DOI: 10.1002/fld.1071.
- Smolarkiewicz, P.K., and W.W. Grabowski (1990), The multidimensional positive definite advection transport algorithm: nonoscillatory option, *J. Comput. Phys.* **86**, 2, 355-375, DOI: 10.1016/0021-9991(90)90105-A.
- Smolarkiewicz, P.K., and J. Szmelter (2009), Iterated upwind schemes for gas dynamics, *J. Comput. Phys.* **228**, 33-54, DOI: 10.1016/j.jcp.2008.08.008.
- Smolarkiewicz, P.K., L.G. Margolin, and A.A. Wyszogrodzki (2001), A class of non-hydrostatic global models, *J. Atmos. Sci.* **58**, 4, 349-364, DOI: 10.1175/1520-0469(2001)058<0349:ACONGM>2.0.CO;2.
- Smoluchowski, M. (1916), Drei Vortraege ueber Diffusion, Brownsche Bewegung und Koagulation von Kolloidteilchen, *Phys. Z.* **17**, 557-585.
- Su, C.-W., S.K. Krueger, P.A. McMurtry, and P.H. Austin (1998), Linear eddy modeling of droplet spectral evolution during entrainment and mixing in cumulus clouds, *Atmos. Res.* **47-48**, 41-58, DOI: 10.1016/S0169-8095(98)00039-8.
- Twomey, S. (1959), The nuclei of natural cloud formation part II: The supersaturation in natural clouds and the variation of cloud droplet concentration, *Pure Appl. Geophys.* **43**, 243-249, DOI: 10.1007/BF01993560.
- Twomey, S. (1974), Pollution and the planetary albedo, *Atmos. Environ.* **8**, 12, 1251-1256, DOI: 10.1016/0004-6981(74)90004-3.
- Twomey, S. (1977), The influence of pollution on the shortwave albedo of clouds, *J. Atmos. Sci.* **34**, 7, 1149-1152, DOI: 10.1175/1520-0469(1977)034<1149:TIOPOT>2.0.CO;2.
- Warner, J. (1969), The microstructure of cumulus cloud. Part II. The effect on droplet size distribution of the cloud nucleus spectrum and updraft velocity, *J. Atmos. Sci.* **26**, 6, 1272-1282, DOI: 10.1175/1520-0469(1969)026<1272:TMOCCP>2.0.CO;2.

Received 16 April 2011

Received in revised form 2 August 2011

Accepted 12 August 2011